

RESEARCH ARTICLE

Precise regulation of pyrrole-type single-atom Mn-N₄ sites for superior pH-universal oxygen reduction

Lei Yan¹ | Liyan Xie¹ | Xi-Lin Wu²  | Mengying Qian² | Jianrong Chen² | Yijun Zhong¹ | Yong Hu^{1,3} 

¹Department of Chemistry, Key Laboratory of the Ministry of Education for Advanced Catalysis Materials, Zhejiang Normal University, Jinhua, Zhejiang, China

²College of Geography and Environmental Science, Zhejiang Normal University, Jinhua, China

³Hangzhou Institute of Advanced Studies, Zhejiang Normal University, Hangzhou, Zhejiang, China

Correspondence

Xi-Lin Wu, College of Geography and Environmental Science, Zhejiang Normal University, 321004 Jinhua, China.
Email: dbwxi@zjnu.cn

Yong Hu, Key Laboratory of the Ministry of Education for Advanced Catalysis Materials, Zhejiang Normal University, Department of Chemistry, Jinhua, 321004 Zhejiang, China.
Email: yonghu@zjnu.edu.cn

Abstract

The study of atomically dispersed metal-nitrogen electrocatalysts is still limited in terms of understanding their catalytic mechanism because of the inability to precisely regulate the coordination number and type of N in combination with the metal elements. Inspired by the high catalytic activity and selectivity of natural enzymes, herein, we have designed and fabricated ultrathin carbon nanosheet-supported Mn single-atom catalysts (SACs) with a precise pyrrole-type Mn-N₄ (PT-MnN₄) configuration using a bio-mimicking strategy. The PT-MnN₄ SACs display outstanding oxygen reduction reaction (ORR) activity, with a half-wave potential ($E_{1/2}$) of 0.88 V (vs. reversible hydrogen electrode RHE) and extremely high stability in alkaline media. Moreover, superior ORR activities are also obtained, $E_{1/2}$ of 0.73 V and 0.63 V in acid and neutral electrolytes, respectively, indicating the efficient pH-universal ORR performances. The assembled zinc-air battery using the PT-MnN₄ SACs as air cathodes exhibits a high peak power density (175 mW cm⁻²) and long-term stability up to 150 h, implying its promising application in metal-air batteries. This study has paved the way toward the rational design and precise regulation of single-atom electrocatalysts.

KEYWORDS

oxygen reduction reaction, pH-universal, pyrrole-type N, single-atom catalysts, Zn-air batteries

1 | INTRODUCTION

Energy conversion devices such as fuel cells and metal-air batteries are promising for obtaining next-generation clean, sustainable, and secure energy.¹⁻⁴ Among the various metal-air batteries, zinc-air batteries (ZABs) are considered one of the most promising candidates for obtaining future portable power devices.⁵

However, the poor activity and stability of the cathodic materials for oxygen reduction reaction (ORR) have remained major obstacles in the practical application of ZABs.⁶ Even though Pt-based materials are generally considered high-efficiency electrocatalysts for ORR, the high cost, scarcity, and poor stability are significant barriers to their widespread application.⁷⁻⁹ Therefore, increasingly more studies have focused on the

This is an open access article under the terms of the Creative Commons Attribution License, which permits use, distribution and reproduction in any medium, provided the original work is properly cited.

© 2021 The Authors. *Carbon Energy* published by Wenzhou University and John Wiley & Sons Australia, Ltd.

development of cost-effective nonnoble metal catalysts for the replacement of the platinum-based catalysts.^{10–12}

In recent years, transition-metal (TM) single-atom catalysts (SACs) have been found to be effective in ORR, including Cr-N₄,¹³ Fe-N₄,¹⁴ Fe-N₅,¹⁵ Co-N₄,¹⁶ Ni-N₄,¹⁷ Cu-N₃,¹⁸ and Zn-N₄¹⁹ sites. These TM SACs have been regarded as the most promising alternatives to commercial Pt/C catalysts. The atomic TM-N moieties in TM SACs are identified as the catalytic active sites for ORR.^{20,21} The different types of TM-N sites possess different electronic structures and adsorption behaviors, leading to diverse catalytic activities. For example, Zhao et al.²² fabricated Cu-N₄ single-atom sites and found that the coordination of pyrrole-type Cu-N₄ was the main active site rather than the Cu-pyridinic-N₄ sites. The pyrrole-type TM-N₄ sites of metalloporphyrins can mimic the catalytic active center of natural metalloenzymes, which were reactive for O₂ activation/reduction processes.²³ Previous experimental and theoretical studies have demonstrated the high catalytic activity and selectivity of metalloporphyrins toward ORR.^{24,25} Moreover, the development of high-purity pyrrole-type TM-N₄ sites can enable an in-depth understanding of the atomic structure–property relationship of TM SACs.^{26,27} For example, Yang et al.²⁸ found that the Fe-pyrrolic N species not only has high activity but can also activate the adjacent C atoms as catalytic sites for ORR. Therefore, metalloporphyrin-like SACs will possess outstanding activity and selectivity in ORR. However, it still remains a challenge to establish an efficient synthetic method to precisely control and synthesize SACs with pyrrole-type TM-N₄ sites, which severely hinders the practical application of TM-N₄ SACs. In addition, to meet the requirements in practical environments, it is worthwhile to develop stable and highly active electrocatalysts in the full pH ranges.^{29,30} However, as far as we know, investigations of the ORR activity of TM SACs at universal pH values are still lacking.³¹

In this study, we present a facile biomimetic-enzyme-induced method for the synthesis of pyrrole-type Mn-N₄ sites (PT-MnN₄) anchored on ultrathin carbon nanosheets by using manganese porphyrin as the Mn source. The isolated PT-MnN₄ sites were confirmed using high-angle annular dark-field scanning transmission electron microscopy (HAADF-STEM) and X-ray absorption spectroscopy (XAS). By mimicking the active center of manganese peroxidase, the precisely regulated PT-MnN₄ sites possess high intrinsic catalytic activity for dioxygen activation and high selectivity for the four-electron-transfer ORR in the full pH ranges. Moreover, the assembled ZABs, using Mn-N₄ SACs as the cathode, also show a large peak power density and a stable discharge curve.

2 | EXPERIMENTAL SECTION

2.1 | Materials and methods

All reagents used in this study are analytical grade, used without further purification. Cyanuric acid (CA) was purchased from Alfa Aesar Chemicals Co., Ltd. Melamine (M) was supplied by Dingshengxin Chemical Industry Co., Ltd. Sodium hydroxide (NaOH), perchloric acid (HCl), and potassium thiocyanate (KSCN) were purchased from Sinopharm Chemical Reagent Co., Ltd. Meso-tetrakis (4-chlorophenyl) porphyrin-Mn (III) chloride was purchased from Beijing InnoChem Science & Technology Co., Ltd.

2.2 | Synthesis of the PT-MnN₄ catalyst

The PT-MnN₄ samples were synthesized via a one-step in situ pyrolysis of a mixture of meso-tetrakis (4-chlorophenyl) porphyrin-Mn (III) chloride and melamine-cyanuric acid (MCA) polymer. Typically, the MCA polymer colloid was formed by mixing 3.0 mmol of M and 3.0 mmol of CA in 40 mL of deionized water under ultrasound for 30 min. The obtained mixture was filtered and washed with deionized water three times, and the resulting MCA polymer colloid was dried at 60°C under vacuum for 12 h. Then, 0.2 g of meso-tetrakis (4-chlorophenyl) porphyrin-Mn (III) chloride was dissolved in 2.0 mL of ethanol and dropwise added in 1.0 g of a solid MCA polymer. The mixture was ground to form a homogeneous powder. Finally, the above mixture powder was subjected to calcination at 450°C for 2 h and then at 700°C for 1 h under an N₂ atmosphere. The heating rate of the calcination process was 5°C min⁻¹. After that, the product was cooled down to room temperature and a black PT-MnN₄ product was obtained.

2.3 | Synthesis of the nitrogen-rich carbon (NC) catalyst

The NC was synthesized by pyrolysis of the pure MCA polymer using the same procedure as described above.

2.4 | Materials characterizations

The crystalline phase was investigated by X-ray diffraction (XRD) using a Bruker D8 Advance diffractometer with Cu-K α radiation. Field-emission scanning electron microscopy (FESEM) was conducted on a Hitachi SU-8010 scanning electron microanalyzer with an

accelerating voltage of 15 kV. Transmission electron microscopy (TEM) and high-resolution TEM (HRTEM) were performed on a JEM-2100F field emission TEM at 200 kV. X-ray photoelectron spectroscopy (XPS) was carried out on an ESCALab MKII X-ray photoelectron spectrometer with Mg K α X-ray as the excitation source. N₂ adsorption isotherms were performed at 77 K on a Micrometrics ASAP 2020. Raman spectroscopy was performed using an InVia-Reflex spectrometer (Renishaw) with 532 nm laser excitation. The Fe K-edge XAFS measurements were performed in a transmission model at the beamline 1W1B of the Beijing Synchrotron Radiation Facility (BSRF, Beijing, China). C K-edge and N K-edge XAS spectra were measured at the beamline U19 of the National Synchrotron Radiation Laboratory (Hefei, China) in the total electron yield mode by collecting the sample drain current under vacuum higher than 10⁻⁷ Pa. Fourier transform infrared spectroscopy (FTIR) spectra were recorded using a Nicolet Nexus 670 spectrometer. The Mn loading of the sample was conducted on an inductively coupled plasma atomic emission spectrometer (ICP-AES; Thermo Fisher Scientific).

The detailed procedure of the electrochemical measurements and the assembly process of the Zn-air battery is described in the [supporting information](#).

3 | RESULTS AND DISCUSSION

The PT-MnN₄ sample is fabricated using meso-tetrakis (4-chlorophenyl) porphyrin-Mn (III) chloride and self-assembled MCA as the precursors. During the calcination process (Figure 1A), the MCA gradually carbonized into nitrogen-rich carbon nanosheets, whereas the pyrrole-type MnN₄ structures in Mn-porphyrin molecules were well maintained and in situ-anchored in the carbon skeletons. The PT-MnN₄ catalyst exhibits a sheet-like structure with a wrinkled surface as observed by the scanning electron microscope (Figure S1). The TEM image (Figure 1B) confirms that the PT-MnN₄ is made of ultrathin carbon nanosheets. The HRTEM (Figure 1C) image displays highly disordered carbon structures without the presence of any Mn nanoparticles. The XRD analysis shows the presence of only one broad peak at ~26° for both pure NC nanosheets and the PT-MnN₄ sample, indicating the presence of graphitic carbons and the absence of metallic Mn-based nanoparticles (Figure 1D). Moreover, the atomic dispersion of Mn atoms on the carbon nanosheets can be observed by the aberration-corrected high-angle annular dark-field scanning TEM (AC HAADF-STEM) (Figure 1E).³² The isolated bright dots of Mn atoms are marked by circles in

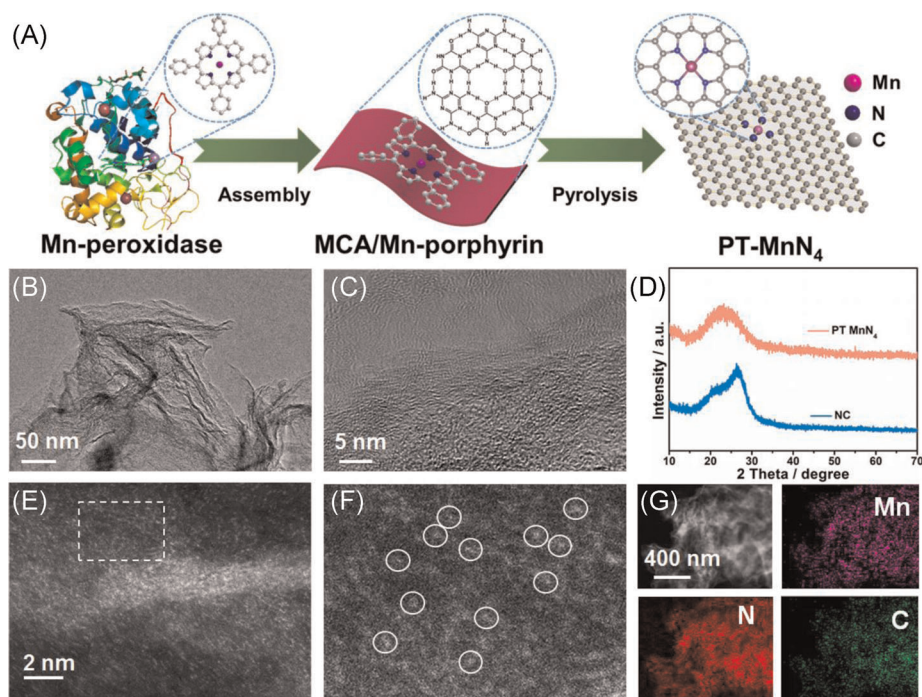


FIGURE 1 (A) Schematic illustration of the fabrication of pyrrole-type (PT)-MnN₄, (B) transmission electron microscopy (TEM) image, (C) High-resolution TEM image of PT-MnN₄, (D) X-ray diffraction patterns of PT-MnN₄ and nitrogen-rich carbon, (E) aberration-corrected high-angle annular dark-field scanning TEM (HAADF-STEM) images, and (F) corresponding selected area of the HAADF-STEM images (the bright dots are highlighted by circles). (G) STEM image and corresponding elemental mapping images of Mn, N, and C for PT-MnN₄

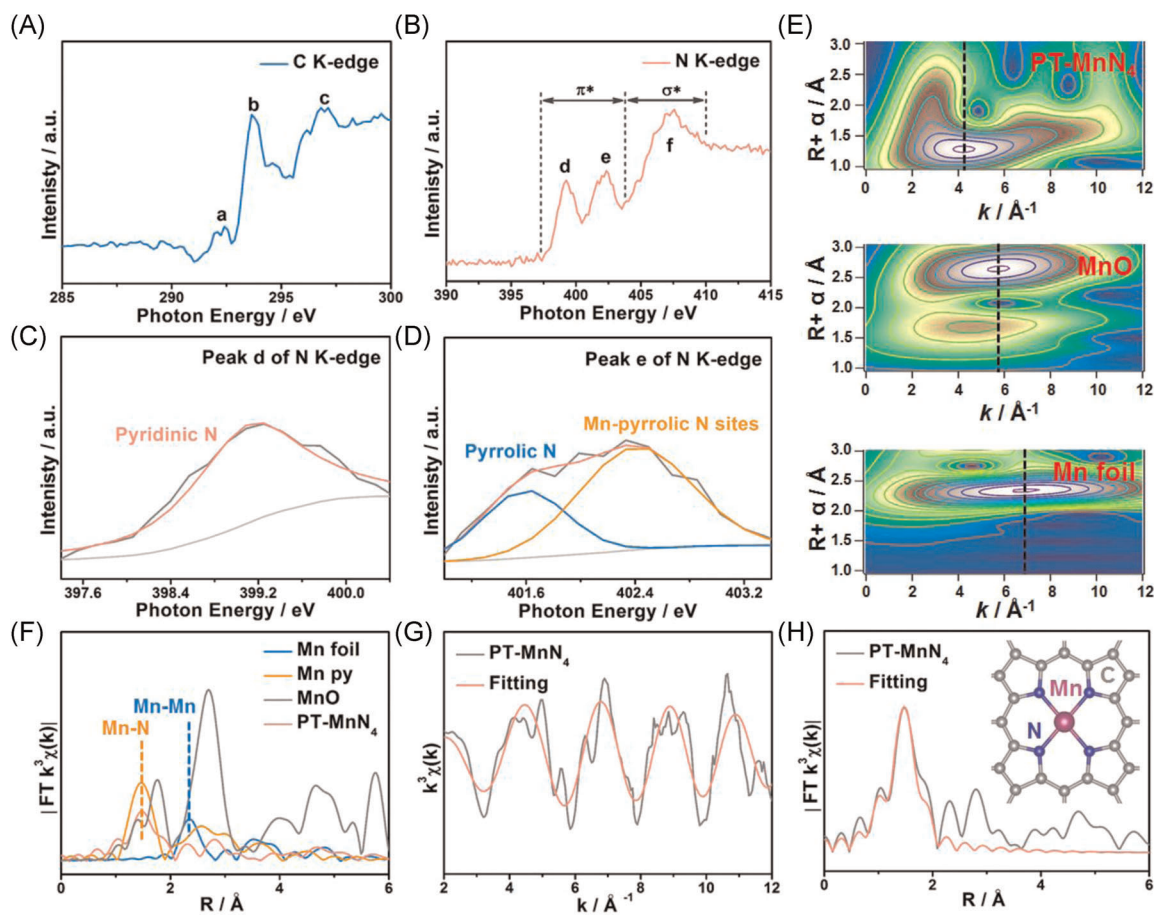


FIGURE 2 (A) C K-edge NEXAFS and (B) N K-edge NEXAFS spectrum of PT-MnN₄. Deconvoluted features of (C) peak d and (D) peak e of the N K-edge spectra. (E) WT-EXAFS of the Mn foil, MnO, and PT-MnN₄. (F) FT-EXAFS curves of PT-MnN₄ and references at the Mn K-edge. (G) *k* space and (H) *R* space FT-EXAFS fitting curves of PT-MnN₄ (Inset: Atomic structure model of PT-MnN₄). EXAFS, extended X-ray absorption fine-structure; FT, Fourier transform; PT, pyrrole-type; WT, wavelet transform

Figure 1F, revealing that the monatomic Mn species are evenly distributed on the carbon support. The energy-dispersive X-ray (EDX) spectroscopy mapping demonstrates that Mn, N, and C elements are homogeneously distributed in the entire PT-MnN₄ sample (Figure 1G). The Mn loading in the PT-MnN₄ sample is measured to be 5.09 wt% by ICP-AES.

The Raman spectra show typical D and G bands located at 1340 and 1590 cm⁻¹, respectively, which is characteristic of graphitic carbons in PT-MnN₄ (Figure S2). At the same time, the ratio of the relative intensities of the D and G bands (*I_D*/*I_G*) is 0.95 for PT-MnN₄, indicating its high degree of graphitization. The graphitic carbons lead to the high electrical conductivity of the PT-MnN₄ sample, which aids electron transportation from the substrates to the Mn single-atom sites. The Brunauer–Emmett–Teller (BET) specific surface area, calculated from the N₂ adsorption–desorption isotherms (Figure S3A), is 598 m² g⁻¹ for the PT-MnN₄ sample. The pore size distribution curve confirms the

mesoporous structure of the PT-MnN₄ sample with a pore volume of 1.54 m³ g⁻¹ (Figure S3B). The large BET-specific surface area and nanoporous structure provide a large number of exposed active sites and accessible diffusion pathways for transportation of ions/molecules, respectively, endowing PT-MnN₄ with high catalytic activity.³³ The FTIR spectra (Figure S4) of the PT-MnN₄ and NC samples show three characteristic peaks, including a broad band at 3423 cm⁻¹ due to the C–OH and N–H stretching vibrations, and the bands at 1606 and 1290 cm⁻¹ correspond to C=N/C=C and C–N stretching modes, respectively.^{34,35} As compared with pure NC, the PT-MnN₄ catalyst displays two new peaks at 830 and 880 cm⁻¹, which are attributed to the metal–ligand (Mn–N) vibrations and the electronic delocalization effect of the metalloporphyrin-like structure, respectively.³⁶ These results suggest the successful fabrication of the PT-MnN₄ sites supported on the NC nanosheets.

The XPS measurement was performed to probe the chemical structure of the samples. As shown in

Figure S5, the survey XPS spectra show the presence of Mn, C, N, and O elements in the PT-MnN₄ sample and C, N, and O elements in pure NC. The corresponding element contents (Table S1) show that the atomic percentages (at%) of Mn, N, C, and O are 1.7%, 12.4%, 79.5%, and 6.4%, respectively. The high-resolution N 1s XPS spectrum (Figure S6A) can be deconvoluted into three peaks, corresponding to pyridinic N (398.5 eV), pyrrolic N (399.7 eV), and graphitic N (401.1 eV).^{37,38} Specifically, as compared with pure NC, the peak of pyrrolic N in the PT-MnN₄ sample shifts to higher binding energy, which may be due to the strong interaction between Mn atoms and pyrrolic N species, indicating the presence of pyrrolic **type** Mn-N bonds.³⁶ As shown in Figure S6B, the contents of the various N species **are** calculated from the area of deconvoluted peaks in the XPS spectra. The content of pyrrolic N is increased from 11.4% for pure NC to 41.4% for the PT-MnN₄ sample, indicating the successful incorporation of the PT-MnN₄ structure into the NC substrates. The high-resolution Mn 2p XPS spectrum (Figure S7) shows the peaks located at 641.0 and 652.8 eV and a specific shake-up satellite peak at 646.0 eV, corresponding to the Mn²⁺ species in the PT-MnN₄ sample.³⁹ Moreover, multiple splitting of the Mn 3s XPS peaks occurs at 5.9 eV, confirming that the valence value of Mn is about 2.^{40,41}

The electronic structure and coordination information of the single-atom Mn sites **is** further investigated by synchrotron XAS. As shown in Figure 2A, the C K-edge XAS spectrum of PT-MnN₄ presents three typical peaks at 292.4 (peak a), 293.6 (peak b), and 296.9 eV (peak c),⁴² owing to the dipole transition of C 1s electrons to the electron orbits of $\pi^*(C=C)$, $\pi^*(C-N-Mn)$, and $\sigma^*(C-C)$,⁴³ respectively. The strong electron coupling effect enables fast and efficient electron transfer across the PT-MnN₄ catalyst, especially to the reactive single-atom Mn-N₄ sites. The N K-edge XAS spectrum of the PT-MnN₄ sample is also dominated by three peaks (Figure 2B), corresponding to the $1s-\pi^*$ transition of the pyridinic nitrogen (peak d) and pyrrolic rings nitrogen (peak e), and the $1s-\sigma^*$ transition of the graphitic nitrogen (peak f).^{43,44} Peak d for pyridinic nitrogen is well fitted by one peak located at 399.2 eV (Figure 2C), which indicates the absence of Mn-pyridinic N coordination in the PT-MnN₄ catalyst. Moreover, peak e for pyrrolic N can be deconvoluted into two peaks located at 401.5 and 402.0 eV, corresponding to the uncoordinated pyrrolic N and Mn-pyrrolic N sites, respectively (Figure 2D).³⁶ These results further demonstrate the successful fabrication of the pyrrolic N-coordinated Mn sites. The PT type Mn-N bonds will induce charge transfer between the Mn sites and the NC substrate, thereby boosting the catalytic activity of the PT-MnN₄ catalyst in ORR.^{45,46}

The Mn K-edge X-ray absorption near-edge structure (XANES) of the PT-MnN₄ sample is shown in Figure S8. The XANES absorption-edge position of the PT-MnN₄ sample **is** close to that of MnO, indicating that the oxidation state of Mn is close to 2+, which is in agreement with the above XPS analysis. The extended X-ray absorption fine-structure (EXAFS) spectra **are** applied to further probe the coordination structure of the single-atom Mn sites. As shown in Figure 2E, the wavelet transform (WT) contour plots of the PT-MnN₄ sample display one intensity maximum at 4.2 Å⁻¹, corresponding to the Mn-N coordination bond. Moreover, the Mn-Mn signals are absent as compared to the MnO and Mn foil references. The Fourier transform (FT) EXAFS spectrum of the PT-MnN₄ sample obviously shows a peak at 1.47 Å for the Mn-N bond (Figure 2F), revealing that the Mn species principally exist in the form of isolated single-atom sites. Least-squares EXAFS curve fitting was conducted to obtain the quantitative structural parameters of the Mn samples (Figures 2G,H and S9). As can be seen from the EXAFS fitting parameters (Table S2), the coordination number of the Mn-N bond is 4.0 and the bond length is 1.95 Å, confirming the formation of Mn-N₄ sites in the PT-MnN₄ sample. These results clearly prove the formation of the PT-MnN₄ single-atom sites. The unique and precisely regulated PT-MnN₄ sites may endow the PT-MnN₄ catalyst with high catalytic activity and selectivity in ORR.

The electrocatalytic performance of the PT-MnN₄ catalyst **is** first investigated using cyclic voltammetry (CV) and linear sweep voltammograms (LSV) methods in a 0.1 M KOH solution. The CV test shows a well-defined cathodic peak for the PT-MnN₄ sample in an O₂-saturated electrolyte, indicating its excellent ORR activity (Figure S10). Furthermore, from the LSV measurements at a rotating rate of 1600 rpm in an alkaline electrolyte (Figure 3A), the PT-MnN₄ catalyst shows a higher onset potential (E_{on}) of 0.95 V and half-wave potential ($E_{1/2}$) of 0.88 V as compared with the commercial Pt/C catalyst ($E_{on} = 0.88$ V and $E_{1/2} = 0.84$ V) and recently reported nonprecious metal ORR electrocatalysts (Table S3). The poor ORR performance of the pure NC ($E_{on} = 0.70$ V, $E_{1/2} = 0.65$ V) reveals that the isolated PT-MnN₄ sites can be recognized as the active sites for ORR. The $E_{1/2}$ of the Mn-porphyrin precursor is 0.60 V (Figure S11). As shown in Figure 3B, the PT-MnN₄ catalyst possesses a high limiting current density (J_L) of 5.80 mA cm⁻² and rapid ORR kinetics with a kinetic current density (J_k) of 12.69 mA cm⁻² at 0.85 V, which are superior to those of the NC and Pt/C catalysts. Besides, the PT-MnN₄ sample shows a much smaller Tafel slope (96 mV dec⁻¹) as compared with the NC (145 mV dec⁻¹) and Pt/C (110 mV dec⁻¹) catalysts, indicating its favorable reaction

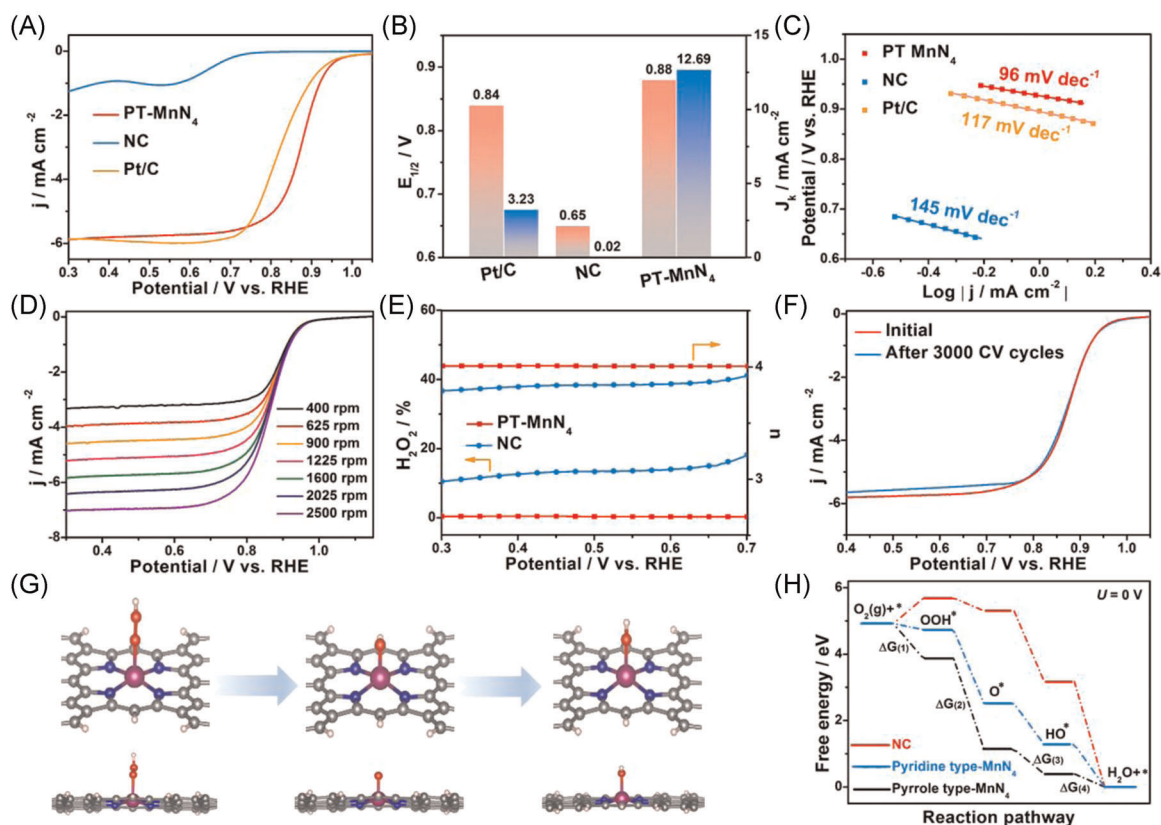


FIGURE 3 (A) LSV curves for ORR of PT-MnN₄, NC, and Pt/C in O₂-saturated 0.1 M KOH. (B) $E_{1/2}$ and J_k of PT-MnN₄, NC, and Pt/C. (C) Tafel plots for ORR. (D) ORR LSV curves on various rotating rates of PT-MnN₄. (E) Electron transfer numbers (n) and peroxide yields of PT-MnN₄ and NC. (F) ORR polarization curves of PT-MnN₄ before and after 3000 CV cycles. (G) Geometric structures of the intermediates OOH*, O*, and OH* for ORR on PT-MnN₄ with an OH* species. (H) Calculated free-energy diagrams for ORR of pyrrole-type MnN₄, pyridine-type MnN₄, and NC. CV, cyclic voltammetry; LSV, linear sweep voltammograms; NC, nitrogen-rich carbon; ORR, oxygen reduction reaction; PT, pyrrole-type

kinetics in the ORR process (Figure 3C). The polarization curves of the PT-MnN₄ catalyst at various rotating speeds are presented in Figure 3D. It can be observed that E_{on} remains constant, whereas J_L increases with an increase in rotating speeds due to the reduced concentration polarization at high rotating speeds. The Koutecky–Levich (K–L) plots of the PT-MnN₄ sample (Figure S12) show good linearity in the range of 0.3–0.7 V, revealing the first-order reaction kinetics for ORR. The catalytic selectivities of the NC and PT-MnN₄ catalysts are evaluated by rotating ring disk electrode (RRDE) measurements. As shown in Figure 3E, the electron transfer number (n) for PT-MnN₄ is about 4.0 and the calculated yield of H₂O₂ is below 3%, demonstrating the excellent ORR selectivity through the four-electron pathways. The interface reactions and kinetics in the ORR are also analyzed by electrochemical impedance spectroscopy (EIS). As shown in Figure S13 and Table S4, PT-MnN₄ displays a smaller charge-transfer resistance (21.82 Ω cm²) than pure NC (102.7 Ω cm²), which allows faster electrons transfer from the NC substrates to the Mn-N₄-active sites. The

electrochemical-active surface areas (ECSA) of PT-MnN₄ and NC measured by the double-layer capacitance (C_{dl}) are determined to be 25.3 and 4.3 mF cm⁻², respectively (Figure S14). The larger ECSA of the PT-MnN₄ catalyst promotes the exposure of more accessible Mn-N₄-active sites for ORR.^{47,48}

The fuel crossover effect and long-term stability are also critical parameters for ORR electrocatalysts. The chronoamperometric ($i-t$) responses of PT-MnN₄ and commercial Pt/C in an O₂-saturated electrolyte are shown in Figure S15. After the addition of methanol to the solution, the current density slightly decreased for PT-MnN₄, but sharply decreased for Pt/C, demonstrating the excellent methanol tolerance of the PT-MnN₄ catalyst. The durability test shows that the current density remains over 91% after 22 h (Figure S16) and only a tiny shift in $E_{1/2}$ is observed after 3000 potential cycles (Figure 3F). Also, the morphology and composition of the PT-MnN₄ catalyst show little change after the OER test, revealing the robust stability of the catalyst (Figure S17). The excellent durability of PT-MnN₄ in an

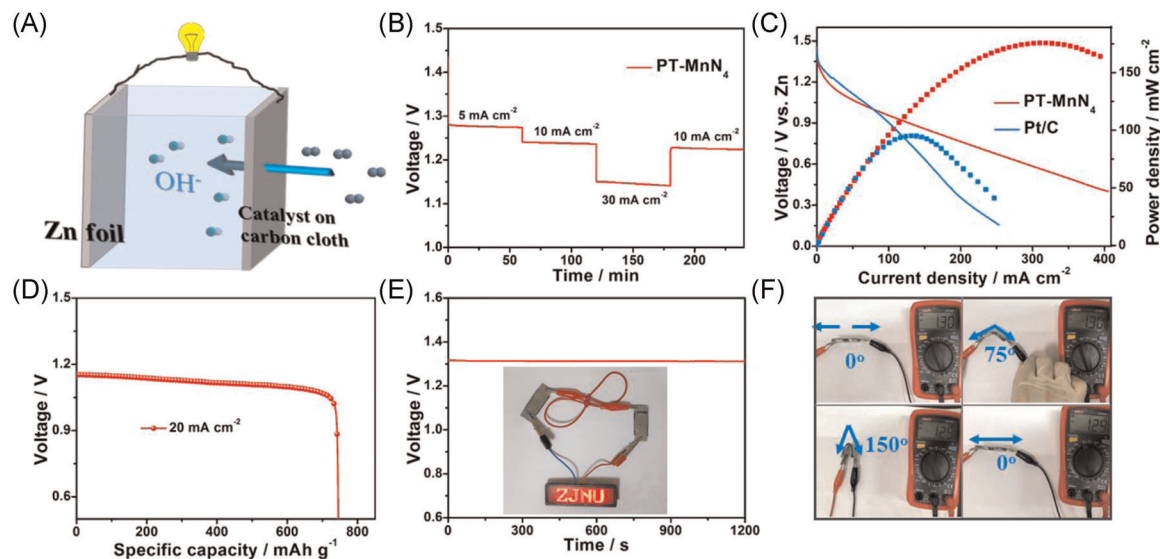


FIGURE 4 (A) Schematic diagram of primary ZABs with PT-MnN₄ as the air cathode. (B) Discharge curves of a PT-MnN₄-based Zn-air battery with current densities from 2 to 30 mA cm⁻². (C) Discharge polarization curves and corresponding power density curve plots of PT-MnN₄-based and commercial Pt/C-based ZABs. (D) Long-term discharge curve under a continuous discharge density of 20 mA cm⁻²; the specific capacity was normalized to consume the Zn mass. (E) All-solid-state ZABs displaying a measured open-circuit voltage of ~1.31 V. Inset: Photograph of a lighted light-emitting diode powered by two all-solid-state ZABs. (F) Photograph of all-solid-state ZABs under different bending angles. PT, pyrrole-type; ZAB, zinc-air batteries

alkaline solution is mainly due to the unique structure of the robust pyrrolic N-coordinated Mn-N₄ sites on the carbon support, preventing the dissolution and aggregation of Mn species.^{20,49} The Mn-N₄-active sites are also identified using SCN⁻ ions as the chemical probe. As shown in Figure S18, the $E_{1/2}$ of the PT-MnN₄ catalyst negatively shifted by 40 mV after adding SCN⁻ to the solution, confirming that the Mn-N₄ single-atom sites are responsible for the high ORR performance.

In addition, PT-MnN₄-mediated ORR performances in acidic (0.5 M H₂SO₄) and neutral (0.1 M PBS) conditions are also explored. It is worth noting that the ORR performance of the PT-MnN₄ catalyst exhibited $E_{1/2}$ of 0.73 V in acid electrolyte and 0.63 V in neutral electrolyte, which is comparable to that of the commercial Pt/C ($E_{1/2}$ = 0.81 V in acid electrolyte and 0.70 V in neutral solution) (Figure S19). Moreover, the ORR activities of the PT-MnN₄ catalyst are comparable to or even surpass the most commonly reported ORR electrocatalysts (Tables S5 and S6). As shown in Figure S20, a small Tafel slope of the PT-MnN₄ catalyst was present in both acidic (186 mV dec⁻¹) and neutral media (195 mV dec⁻¹), suggesting a faster ORR kinetics. On the basis of the K-L equation, the catalytic ORR process follows a first-order ORR reaction kinetics as well as a 4e process (Figure S21) in both acidic and neutral media, which was further confirmed by the RRDE measurements (Figure S22). The average n was determined to be 3.9, and the H₂O₂ yield was less than 3% in the acid solution, whereas in neutral

media, these values were about 3.80% and 8%, respectively. Therefore, the PT-MnN₄ catalyst follows the 4e⁻ mechanism in both acidic and neutral media. Furthermore, after 3000 CV scans, the PT-MnN₄ catalyst shows a negligible decrease, which further demonstrated the good stability of the catalyst in acidic and neutral conditions (Figure S23).

The influence of the PT-MnN₄ structure on the ORR process is theoretically studied using density functional theory (DFT) calculations.⁴² Figure 3G shows the atomic interface configuration details of the four-electron ORR reaction steps on a PT-MnN₄ catalyst. First, O₂ molecules are adsorbed on the central Mn-active sites and protonated to form OOH*. Second, the OOH* is dissociated into O* and OH*. Finally, the OH* is further converted into an H₂O molecule. The Gibbs free energies for reaction steps of the PT-MnN₄-mediated ORR process are calculated (see details in the Supporting Information). The free-energy diagrams at a potential $U = 0$ V along with the reaction pathways are shown in Figure 3H. The calculated Gibbs free energies are listed in Table S7. For NC, the conversion from O₂ into *OOH is an energetically uphill process, which is not thermodynamically favored. For PT-MnN₄, the value of $\Delta G(4)$ (-0.39 eV) is more positive than $\Delta G(1)$ (-1.06 eV), $\Delta G(2)$ (-2.72 eV), and $\Delta G(3)$ (-0.74 eV), indicating that the reaction pathway from OH* to H₂O is the potential-determining step (PDS). On the one hand, the Gibbs free-energy difference between O₂ and OOH* of pyrrole-type MnN₄ is lower than that of pyridine-type MnN₄ and NC, suggesting the

pyrrole-type MnN_4 -preferable oxygen adsorption for the ORR.⁵⁰ On the other hand, the pyrrole-type MnN_4 displays much lower PDS energies— $\Delta G(4)$ (−0.39 eV)—compared with pyridine-type MnN_4 — $\Delta G(1)$ (−0.19 eV)—and the NC catalyst— $\Delta G(1)$ (0.77 eV), confirming the high catalytic activity of the pyrrole-type MnN_4 single-atom sites. These results provide an atomic-scale understanding of the high electrocatalytic activity of the PT- MnN_4 catalyst.

Zinc–air batteries are constructed using a PT- MnN_4 -loaded carbon-fiber paper (CFP) as the air electrode and a Zn foil as the anode in a 6 M KOH electrolyte (Figure 4A). For comparison, a ZAB using a commercial Pt/C catalyst is also constructed using the same procedure. As shown in Figure S24, the open-circuit voltage (OCV) of the PT- MnN_4 -based ZAB is as high as 1.45 V, larger than the OCV of Pt/C (1.43 V), suggesting good intrinsic catalytic performance of the PT- MnN_4 catalyst. According to Figure 4B, the PT- MnN_4 -based ZAB shows a small voltage drop at the current density range of 5–30 mA cm^{-2} . More importantly, the discharge can be resumed quickly once the current density is tuned to 10 mA cm^{-2} , suggesting its good reversibility. From the polarization and power density curves (Figure 4C), it can be observed that the PT- MnN_4 -based ZAB achieved a maximum power density of 176 mW cm^{-2} at a current density of 310 mA cm^{-2} , which is significantly higher than that of the Pt/C-based ZAB (96 mW cm^{-2}). When discharged at a current density of 20 mA cm^{-2} , the PT- MnN_4 -based ZAB shows a specific capacity of 750 mAh g Zn^{-1} (Figure 4D), comparable to the Pt/C-based ZAB (specific capacity, 824 mAh g Zn^{-1}) (Figure S25). As shown in Table S8, the PT- MnN_4 -based ZAB exhibits comparable performance to that of the state-of-the-art non-precious-metal catalysts. Moreover, the PT- MnN_4 -based ZAB maintains high stability up to 150 h when discharging at a current density of 10 mA cm^{-2} (Figure S26), suggesting its outstanding long-term durability. The PT- MnN_4 -based all-solid-state ZAB shows an OCV of ~1.31 V, and two of the ZABs can easily light the light-emitting diodes (Figure 4E,D). The all-solid-state ZAB also possesses stable mechanical flexibility even when it is bent at various angles (Figure 4F), implying the excellent application potential of the PT- MnN_4 -based ZAB in energy conversion devices. Based on the above results, the excellent electrocatalytic performance of the PT- MnN_4 catalyst can be attributed to the following factors: (1) the high-purity PT- MnN_4 sites significantly promote the conversion of O_2 into OOH^* and enhance the intrinsic activity for ORR, (2) the existence of massive mesopores in the ultrathin NC support considerably promotes the utilization of more accessible active sites,^{51,52} and (3) the combination of high intrinsic catalytic activity and enriched catalytic sites of PT- MnN_4 markedly accelerates the ORR processes and a high power density is achieved when it is assembled into ZABs.^{53,54}

4 | CONCLUSION

In summary, for the first time, PT- MnN_4 single-atom sites are constructed using a facile biomimetic-enzyme-induced strategy. Due to the advantages of the regulated electronic structures and high accessibility of the PT- MnN_4 -active sites, the as-obtained catalyst exhibits excellent ORR activity, with an E_{on} of 0.95 V and $E_{1/2}$ of 0.88 V (vs. RHE) in alkaline media. Moreover, it also shows high ORR activity and stability in acid and neutral media. Precisely regulated PT- MnN_4 sites are identified as the active centers in ORR using XAS and DFT calculations. Significantly, ZABs, by using the PT- MnN_4 catalyst as the air cathode, can yield a large peak power density (175 mW cm^{-2}) and stable discharging up to 150 h. This study will open up new avenues for the rational design and precise regulation of single-atom electrocatalysts for energy conversions.

ACKNOWLEDGMENTS

Lei Yan and Lian Xie contributed equally to this study. The authors thank Shenzhen HUASUAN Technology Co. LTD for helping with the density functional theory (DFT) calculations. Yong Hu acknowledges the financial support from the Independent Designing Scientific Research Project of Zhejiang Normal University (2020ZS03) and the Zhejiang Provincial Ten Thousand Talent Program (2017R52043). Xilin Wu acknowledges the financial support from the Zhejiang Province Basic Public Welfare Research Project (LGF19B070006). Jianrong Chen was supported by the National Natural Science Foundation of China (No. 21775138).

ORCID

Xi-Lin Wu  <https://orcid.org/0000-0002-0056-7782>

Yong Hu  <http://orcid.org/0000-0003-3777-167X>

REFERENCES

1. Yang D, Chen D, Jiang Y, et al. Carbon-based materials for all-solid-state zinc–air batteries. *Carbon Energy*. 2020;3(1):50–65.
2. Xu Q, Pang H, Xue H, Li Q, Zheng S. A highly alkaline-stable metal oxide@metal–organic framework composite for high-performance electrochemical energy storage. *Nat Sci Rev*. 2020; 73(2):305–314.
3. Tan P, Chen B, Xu H, et al. Flexible Zn- and Li-air batteries: recent advances, challenges, and future perspectives. *Energy Environ Sci*. 2017;10(10):2056–2080.
4. Xia BY, Yan Y, Li N, Wu HB, Lou XW, Wang X. A metal-organic framework-derived bifunctional oxygen electrocatalyst. *Nat Energy*. 2016;1(1):1.
5. An L, Zhang Z, Feng J, et al. Heterostructure-promoted oxygen electrocatalysis enables rechargeable zinc–air battery with neutral aqueous electrolyte. *J Am Chem Soc*. 2018;140(50): 17624–17631.
6. Zhang K, Zhang Y, Zhang Q, et al. Metal-organic framework-derived Fe/Cu-substituted Co nanoparticles embedded in

- CNTs-grafted carbon polyhedron for Zn-air batteries. *Carbon Energy*. 2020;2(2):283-293.
- Yu XY, Yu L, Lou XW. Metal sulfide hollow nanostructures for electrochemical energy storage. *Adv Energy Mater*. 2016; 6(3):1501333.
 - Nie Y, Li L, Wei Z. Recent advancements in Pt and Pt-free catalysts for oxygen reduction reaction. *Chem Soc Rev*. 2015; 44(8):2168-2201.
 - Lv S, Hu H, Hou Y, et al. Graphene layers-wrapped Fe/Fe₅C₂ nanoparticles supported on n-doped graphene nanosheets for highly efficient oxygen reduction. *Adv Energy Mater*. 2018; 8(9):1702476.
 - Lu W, Shen J, Zhang P, Zhong Y, Hu Y, Lou X. Construction of CoO/Co-Cu-S hierarchical tubular heterostructures for hybrid supercapacitors. *Angew Chem Int Ed*. 2019;58(43): 15441-15447.
 - Wang H, Ye W, Yang Y, Zhong Y, Hu Y. Zn-ion hybrid supercapacitors: achievements, challenges and future perspectives. *Nano Energy*. 2021;85:105942.
 - Hu E, Feng Y, Nai J, Zhao D, Hu Y, Lou XW. Construction of hierarchical Ni-Co-P hollow nanobricks with oriented nanosheets for efficient overall water splitting. *Energy Environ Sci*. 2018;11(4):872-880.
 - Luo E, Zhang H, Wang X, et al. Single-atom Cr-N₄ sites designed for durable oxygen reduction catalysis in acid media. *Angew Chem Int Ed*. 2019;58(36):12469-12475.
 - Wang Y, Tang YJ, Zhou K. Self-adjusting activity induced by intrinsic reaction intermediate in Fe-N-C single-atom catalysts. *J Am Chem Soc*. 2019;141(36):14115-14119.
 - Lu Q, Zou X, Liao K, et al. Direct growth of ordered N-doped carbon nanotube arrays on carbon fiber cloth as a free-standing and binder-free air electrode for flexible quasi-solid-state rechargeable Zn-Air batteries. *Carbon Energy*. 2020;2(3): 461-471.
 - Sun X, Sun S, Gu S, et al. High-performance single atom bifunctional oxygen catalysts derived from ZIF-67 superstructures. *Nano Energy*. 2019;61:245-250.
 - Cai Z, Du P, Liang W, et al. Single-atom-sized Ni-N₄ sites anchored in three-dimensional hierarchical carbon nanostructures for the oxygen reduction reaction. *J Mater Chem A*. 2020;8(30):15012-15022.
 - Ma S, Han Z, Leng K, et al. Ionic exchange of metal-organic frameworks for constructing unsaturated copper single-atom catalysts for boosting oxygen reduction reaction. *Small*. 2020; 16(23):2001384.
 - Song P, Luo M, Liu X, et al. Zn single-atom catalyst for highly efficient oxygen reduction reaction. *Adv Funct Mater*. 2017; 27(28):1700802.
 - Lu Z, Wang B, Hu Y, et al. An isolated zinc-cobalt atomic pair for highly active and durable oxygen reduction. *Angew Chem Int Ed*. 2019;58(9):2622-2626.
 - Tang T, Jiang WJ, Liu XZ, et al. Metastable rock salt oxide-mediated synthesis of high-density dual-protected M@NC for long-life rechargeable zinc-air batteries with record power density. *J Am Chem Soc*. 2020;142(15):7116-7127.
 - Zhao K, Nie X, Wang H, et al. Selective electroreduction of CO₂ to acetone by single copper atoms anchored on N-doped porous carbon. *Nat Commun*. 2020;11(1):2455.
 - Wei PJ, Yu GQ, Naruta Y, Liu JG. Covalent grafting of carbon nanotubes with a biomimetic heme model compound to enhance oxygen reduction reactions. *Angew Chem Int Ed*. 2014; 53(26):6659-6663.
 - Yamazaki S-I. Metalloporphyrins and related metallomacrocycles as electrocatalysts for use in polymer electrolyte fuel cells and water electrolyzers. *Coord Chem Rev*. 2018;373: 148-166.
 - Kosa M, Levy N, Elbaz L, Major DT. Theoretical study of the electrocatalytic reduction of oxygen by metalcorroles. *J Phys Chem C*. 2018;122(31):17686-17694.
 - Liu KX, Wu G, Wang GF. Role of local carbon structure surrounding fen4 sites in boosting the catalytic activity for oxygen reduction. *J Phys Chem C*. 2017;121(21):11319-11324.
 - Liu J, Song P, Xu WL. Structure-activity relationship of doped-nitrogen (N)-based metal-free active sites on carbon for oxygen reduction reaction. *Carbon*. 2017;115:763-772.
 - Yang L, Cheng D, Xu H, et al. Unveiling the high-activity origin of single-atom iron catalysts for oxygen reduction reaction. *Proc Natl Acad Sci U S A*. 2018;115(26):6626-6631.
 - Wei X, Luo X, Wang H, et al. Highly-defective Fe-N-C catalysts towards pH-universal oxygen reduction reaction. *Appl Catal B-Environ*. 2020;263:118347.
 - Xu Y, Zhang H, Zhang P, Lu M, Xie X, Huang L. In situ exsolved Co components on wood ear-derived porous carbon for catalyzing oxygen reduction over a wide pH range dagger. *J Mater Chem A*. 2021;9(17):10695-10703.
 - Zhang J, Yang H, Liu B. Coordination engineering of single-atom catalysts for the oxygen reduction reaction: a review. *Adv Energy Mater*. 2020;11(3):2002473.
 - Chen F, Wu XL, Shi C, et al. Molecular engineering toward pyrrolic N-rich M-N₄ (M = Cr, Mn, Fe, Co, Cu) single-atom sites for enhanced heterogeneous fenton-like reaction. *Adv Funct Mater*. 2021;31(13):202007877.
 - Xiao P, Wang P, Li H, et al. New insights into bisphenols removal by nitrogen-rich nanocarbons: synergistic effect between adsorption and oxidative degradation. *J Hazard Mater*. 2018;345:123-130.
 - Xu L, Tian Y, Deng D, et al. Cu Nanoclusters/FeN₄ amorphous composites with dual active sites in N-doped graphene for high-performance Zn-air batteries. *ACS Appl Mater Inter*. 2020;12(28):31340-31350.
 - Zhang Z, Dou M, Ji J, Wang F. Phthalocyanine tethered iron phthalocyanine on graphitized carbon black as superior electrocatalyst for oxygen reduction reaction. *Nano Energy*. 2017; 34:338-343.
 - Zhang N, Zhou T, Chen M, et al. High-purity pyrrole-type FeN₄ sites as a superior oxygen reduction electrocatalyst. *Energy Environ Sci*. 2020;13(1):111-118.
 - Yu P, Wang L, Sun F, et al. Co nanoislands rooted on Co-N-C nanosheets as efficient oxygen electrocatalyst for Zn-air batteries. *Adv Mater*. 2019;31(30):1901666.
 - Yin SH, Yang J, Han Y, et al. Construction of highly active metal-containing nanoparticles and FeCo-N₄ composite sites for the acidic oxygen reduction reaction. *Angew Chem Int Ed*. 2020;59(49):21976-21979.
 - Guo Z, Xie Y, Xiao J, et al. Single-atom Mn-N₄ site-catalyzed peroxone reaction for the efficient production of hydroxyl

- radicals in an acidic solution. *J Am Chem Soc.* 2019;141(30):12005-12010.
40. Gu Y, Yan G, Lian Y, et al. Mn III-enriched α -MnO₂ nanowires as efficient bifunctional oxygen catalysts for rechargeable Zn-air batteries. *Energy Stor Mater.* 2019;23:252-260.
 41. Tan Q, Li X, Zhang B, et al. Valence engineering via in situ carbon reduction on octahedron sites Mn₃O₄ for ultra-long cycle life aqueous zn-ion battery. *Adv Energy Mater.* 2020;10(38):2001050.
 42. Shang H, Sun W, Sui R, et al. Engineering isolated Mn-N₂C₂ atomic interface sites for efficient bifunctional oxygen reduction and evolution reaction. *Nano Lett.* 2020;20(7):5443-5450.
 43. Chen P, Zhang N, Wang S, et al. Interfacial engineering of cobalt sulfide/graphene hybrids for highly efficient ammonia electrosynthesis. *Proc Natl Acad Sci.* 2019;116(14):6635-6640.
 44. Wu K, Zhang L, Yuan Y, et al. An iron-decorated carbon aerogel for rechargeable flow and flexible zn-air batteries. *Adv Mater.* 2020;32(32):2002292.
 45. Amiin IS, Liu X, Pu Z, et al. From 3D ZIF nanocrystals to Co-N_x/C nanorod array electrocatalysts for ORR, OER, and Zn-air batteries. *Adv Funct Mater.* 2018;28(5):1704638.
 46. Masa J, Xia W, Muhler M, Schuhmann W. On the role of metals in nitrogen-doped carbon electrocatalysts for oxygen reduction. *Angew Chem Int Ed.* 2015;54(35):10102-10120.
 47. Hu E, Ning J, Zhao D, et al. A room-temperature postsynthetic ligand exchange strategy to construct mesoporous Fe-doped cop hollow triangle plate arrays for efficient electrocatalytic water splitting. *Small.* 2018;14(14):1704233.
 48. Yan L, Wang H, Shen J, Ning J, Zhong Y, Hu Y. Formation of mesoporous Co/CoS/Metal-N-C@S, N-codoped hairy carbon polyhedrons as an efficient trifunctional electrocatalyst for Zn-air batteries and water splitting. *Chem Eng J.* 2021;403:126385.
 49. Mun Y, Lee S, Kim K, et al. Versatile strategy for tuning ORR activity of a single Fe-N₄ site by controlling electron-withdrawing/donating properties of a carbon plane. *J Am Chem Soc.* 2019;141(15):6254-6262.
 50. Li J, Chen M, Cullen DA, et al. Atomically dispersed manganese catalysts for oxygen reduction in proton-exchange membrane fuel cells. *Nat Catal.* 2018;1(12):935-945.
 51. Wu M, Zhang G, Hu Y, et al. Graphitic-shell encapsulated FeNi alloy/nitride nanocrystals on biomass-derived N-doped carbon as an efficient electrocatalyst for rechargeable Zn-air battery. *Carbon Energy.* 2020;3(1):176-187.
 52. Wu J, Liu B, Fan X, et al. Carbon-based cathode materials for rechargeable zinc-air batteries: from current collectors to bifunctional integrated air electrodes. *Carbon Energy.* 2020;2(3):370-386.
 53. Li X, Wei J, Li Q, et al. Nitrogen-doped cobalt oxide nanostructures derived from cobalt-alanine complexes for high-performance oxygen evolution reactions. *Adv Funct Mater.* 2018;28(23):1800886.
 54. Yan L, Xu Z, Hu W, Ning J, Zhong Y, Hu Y. Formation of sandwiched leaf-like CNTs-Co/ZnCo₂O₄@NC-CNTs nanohybrids for high-power-density rechargeable Zn-air batteries. *Nano Energy.* 2021;82:105710.

SUPPORTING INFORMATION

Additional Supporting Information may be found online in the supporting information tab for this article.

How to cite this article: Yan L, Xie L, Wu X-L, et al. Precise regulation of pyrrole-type single-atom Mn-N₄ sites for superior pH-universal oxygen reduction. *Carbon Energy.* 2021;1-10.
<https://doi.org/10.1002/cey2.135>